Task-Driven Imaging on an Experimental CBCT Bench: Tube Current Modulation and Regularization Design

Grace J. Gang, Wenying Wang, Aswin Mathews, and J. Webster Stayman

Abstract— **This work investigates the prospective design of tube current modulation (TCM) and regularization for penalized-likelihood (PL) reconstruction on an experimental cone-beam CT (CBCT) bench. The design follows a task-driven imaging framework where a three-dimensional (3D) scout was first acquired and used as the anatomical model. A task-driven optimization process was then performed over a low-dimensional parameter space using the task-based image quality metric, detectability index (d'), as the objective function. Detectability index was computed as a function of a pre-specified imaging task and the noise and resolution properties of the reconstructed image predicted by a system model. The optimal combination of TCM and regularization was then used for subsequent data acquisition and reconstruction. The design was performed for a cluster discrimination task consisting of three 1/16" acetal spheres placed within a 3D printed elliptical phantom. Images were acquired on an experimental cone-beam CT system where TCM was achieved through a custom-modified interface for pulse width modulation at fixed tube current and tube voltage. In addition to imaging strategies dictated by the task-driven imaging framework, scans with no TCM (unmodulated) and conventional TCM based on variance minimization in FBP reconstruction were also performed at the same total exposure for comparison. The task-driven imaging framework suggests that the optimal TCM for PL reconstruction has the opposite trend from that for FBP. Qualitative analysis of reconstructions for each strategy strongly support the trend of theoretical d' values. The TCM profile that is optimal for FBP performs poorly on low exposure data when used for PL. Task-driven strategies outperform the other methods providing the greatest number of visible stimuli in at low exposures. Initial investigations in this work show in experimental data that current, clinically implemented TCM strategies designed for FBP reconstruction can be suboptimal for model-based iterative reconstruction methods. Imaging performance is coupled to both the data acquisition and reconstruction methods, suggesting that current clinical protocols should be re-evaluated for newer model-based reconstruction approaches. The task-driven imaging framework offers a promising approach for prospectively prescribing acquisition and reconstruction in a manner that maximizes task-based imaging performance for a given exposure.**

Index Terms— **Computed tomography, detectability index, image quality, imaging task, model-based iterative reconstruction, regularization design, task-driven imaging.**

I. Introduction

Techniques for reducing radiation dose while maintaining image quality have been a major research focus in computed tomography (CT) and cone-beam CT (CBCT) [1]. Such research efforts encompass the entire imaging chain, from knowledgeable system design [2], hardware solutions (e.g., fluence modulation devices) [3]–[5], acquisition protocols (tube current modulation or kV selection) [6], [7], to imaging processing and advanced model-based iterative reconstruction (MBIR) algorithms [8]–[10]. Recently, task-driven imaging frameworks have been proposed to prospectively design patient-specific acquisition and reconstruction protocols in order to maximize task-based imaging performance at a specific exposure level [11], [12]. Such frameworks rely on an anatomical model provided by a prior image (e.g., a low dose 3D scout) and use detectability index, d', for a specified imaging task (or tasks) as the objective function in an optimization loop to identify the optimal combination of imaging parameters.

The utility of the task-driven approach has been demonstrated in a number of imaging scenarios, including trajectory design in robotic C-arms [11], MBIR regularization design [13], and joint optimization of tube current modulation (TCM) and MBIR regularization [14].

The latter work on TCM and MBIR found a significant disparity between traditional TCM approaches and what is optimal for MBIR [14]. Specifically, The TCM patterns routinely adopted in diagnostic CT scans have been generally designed for FBP reconstruction based on a noise objective – e.g., the minimum variance solution proposed by Gies et al. and Harpen [15], [16]. Such designs are also often close to optimal in terms of task-based imaging performance as well when FBP is used [12]. However, applying the task-driven imaging framework, the studies in [14] suggest that the TCM pattern optimal for MBIR may in fact be the opposite to that for FBP. These previous studies of the task-driven framework have, thus far, been focused on simulation studies. In this work, we investigate the feasibility of task-driven imaging on an experimental cone-beam CT system. In particular, we seek to validate the results of tube current modulation and regularization optimization for MBIR in real data on an experimental CBCT imaging bench. The optimization will be applied to a discrimination task in an elliptical water phantom. Results from the task-driven strategy will be compared with conventional TCM patterns designed for FBP reconstructions.

II. Task-Driven Imaging Framework

A. Overview of the task-driven workflow

Theoretical aspects of the task-driven imaging framework have be detailed in previous work [14], [17] and will be briefly summarized below. The presumed task-driven workflow for

This work is supported in part by NIH grant U01EB018758. G. J. Gang, W. Wang, A. Mathews, and J. W. Stayman are with the Department of Biomedical Engineering, Johns Hopkins University, Baltimore, MD 21205 USA (e-mail: grace.j.gang@jhu.edu, web.stayman@jhu.edu).

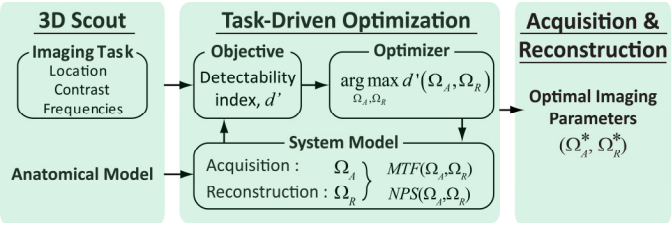

Fig.1. Workflow for the task-driven imaging framework.

experimental implementation of the framework is provided in Fig.1. First, a (low-dose) 3D scout image is acquired to provide a patient-specific anatomical model. The imaging task is presumed to be well-defined and may be identified based on the scout volume, or be constructed based on the suspected lesion or disease prevalence. For diagnostic imaging scenarios, the imaging task typically includes uncertainties in the shape, size and location of the stimulus. There are various ways to incorporate such uncertainties including the use of multi-task objectives, generalized task functions, etc. In this work, we will focus on a single, well-defined task. The task-based image quality metric is be calculated as a function of the spatial resolution (in terms of the modulation transfer function) and noise (in terms of the noise power spectrum) in the reconstructed image. These quantities are naturally dependent on the acquisition and reconstruction parameters we seek to optimize through a well-specified system model. The task-based image quality metric serves as the objective function to an optimization algorithm which identifies the optimal combination of imaging parameters for subsequent imaging procedures.

In this work, we focus on the joint optimization of TCM and regularization for a binary classification task at a known location in the object. In this case, detectability index can be directly used as the objective function in the optimization. A non-prewhitening observer model was adopted, permitting the following definition of d':

$$d_j'^2(\Omega_A,\Omega_R) = \frac{\left[\int\int\int T_j^2(\Omega_A,\Omega_R)W_{Task}^2 df_x df_y df_z\right]^2}{\int\int\int S_j(\Omega_A,\Omega_R)T_j^2(\Omega_A,\Omega_R)W_{Task}^2 df_x df_y df_z} \quad (1)$$

where the subscript j denotes the location of the stimulus, W_{Task} is the task function equal to the difference in the Fourier transforms of the two hypotheses.

B. Quadratic penalized-likelihood (PL) reconstruction

This work focused on a penalized-likelihood reconstruction algorithms whose objective may be written as:

$$\hat{\mu} = \underset{\mu}{\operatorname{argmax}}[\log L(\mu; y) - \beta R(\mu)] \quad (2)$$

where vector $\hat{\mu}$ is the reconstructed volume of attenuation estimates, μ is the argument for optimization, $L(\mu; y)$ denotes the likelihood term, and β is the penalty strength controlling the relative weight of the penalty function, $R(\mu)$. The measurement vector, y, is assumed to be composed of independent Poisson variables that follows the simplified forward model:

$$\bar{y} = I_0(\theta)e^{-\mathbf{A}\mu} \quad (3)$$

where $\mathbf{A}$ is the forward projector and I_0 is the barebeam fluence which may vary as a function of the projection angle, θ. A quadratic roughness penalty was used in this work, and has the general form:

$$\beta R(\mu) = \sum_j \frac{1}{2}\beta_j \sum_{k\in\mathcal{N}_j} r_{jk}\xi_{jk}\ \frac{1}{2}\left(\mu_j - \mu_k\right)^2 \quad (4)$$

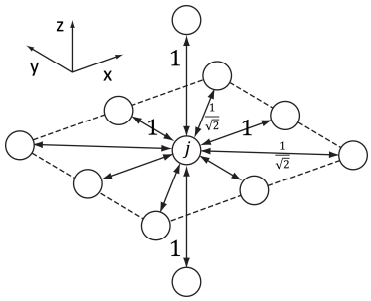

Fig.2. Illustration of the neighborhood around voxel j over which the penalty function is active. Distance weighting factors ξ_{jk} are overlaid for each voxel pair. In conventional weighting schemes, $r_{jk} = 1$ for all directions.

where j and k denote voxel locations, $\mathcal{N}_j$ is the neighborhood around voxel j where the penalty function is applied, and ξ_{jk} denotes a (inverse) distance weighting factor between voxels j and k. This work considers an eight-neighborhood or four voxel pairs in-plane (x-y) and two neighbors out-of-plane (z), as illustrated in Fig. 2.

In addition to the penalty strength parameter, β_j, Eq. (4) includes an addition weighting factor, r_{jk}, for each voxel pair. While usually equal to 1 for all voxel pairs, r_{jk} is allowed to vary in this investigation, enabling additional freedom in shaping the isotropy/anisotropy of the local noise and resolution properties. While this parameterization of the penalty includes redundancies, the form of Eq. (4) separates the effect of overall penalty strength (β_j) and directionality of the noise and resolution (r_{jk}).

C. Expressions for local noise and resolution properties

Since the optimization process involves many evaluations of the objective function, efficient calculations of the MTF and NPS are necessary for computationally feasible implementation of the framework. Towards this end, we adopted a combination of Fourier and analytical approximations of the MTF and NPS detailed in Refs [18]–[20]. Briefly, the local MTF and NPS at voxel j can be written as:

$$T_j \approx \frac{\mathcal{F}\{\mathbf{A}^T D\{\bar{y}(\mu)\}\mathbf{A}e_j\}}{\mathcal{F}\{\mathbf{A}^T D\{\bar{y}(\mu)\}\mathbf{A}e_j + \beta\mathbf{R}e_j\}} \quad 5(a)$$

$$S_j \approx \frac{\mathcal{F}\{\mathbf{A}^T D\{\bar{y}(\mu)\}\mathbf{A}e_j\}}{\left|\mathcal{F}\{\mathbf{A}^T D\{\bar{y}(\mu)\}\mathbf{A}e_j + \beta\mathbf{R}e_j\}\right|^2} \quad 5(b)$$

where $\mathcal{F}\{\cdot\}$ denotes the discrete Fourier transform, $D\{\cdot\}$ is a diagonal matrix whose diagonal elements correspond to its vector input, $\mathbf{A}^T D\{\bar{y}(\mu)\}\mathbf{A}$ and $\mathbf{R}$ are the Hessians of the data-fit term and penalty term, respectively, and e_j is a unit vector at voxel j. For experimental data where the mean measurement $[\bar{y}(\mu)]$ is not available, the noisy measurement, y, can be used as a substitute. Though this estimate is inexact, because $\boldsymbol{A}^T$ and $\boldsymbol{A}$ are both smoothing operators, the predictors are fairly robust against the effects of noise in y.

D. Imaging parameters and optimization algorithm

We investigate the joint optimization of TCM and regularization in this work. In order to reduce the dimensionality of the optimization, TCM was represented as a linear combination of shifted Gaussian basis functions, $\mathcal{B}_n(\theta)$, shown in Fig. 3:

$$I_0(\theta) = \sum_n^N \Omega_n \mathcal{B}_n(\theta) \ \text{ for } \theta \in [0, 2\pi] \quad (6)$$

where Ω_n denotes the set of coefficients to be optimized. The centers of the basis functions are evenly spaced along θ, and the standard deviation was chosen such that $I_0(\theta)$ can be as a close

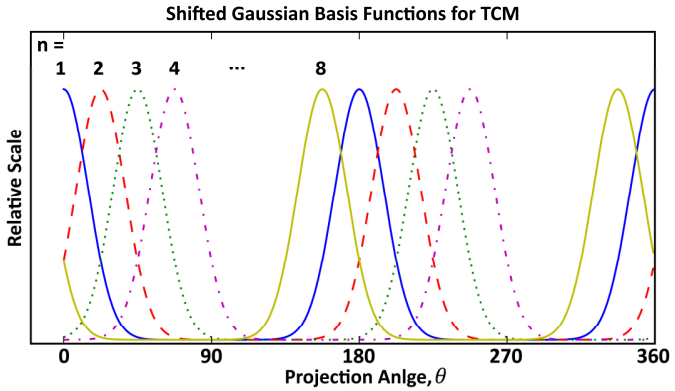

Fig.3. Eight Gaussian basis functions were used to parameterize TCM in order to reduce the dimensionality of the parameters.

to flat as possible when all Ω_ns are equal. In addition, under a parallel beam approximation, projections 180° are assumed to have the same fluence. As a dose constraint, the total fluence across all projections was constrained to a fixed value for all TCM profiles, i.e.,

$$\sum_\theta I_0(\theta) = I_0^{tot}. \quad (7)$$

In addition to TCM, both β_j and r_{jk} from Eq.(4) were optimized. To separate the effect of overall penalty strength (β_j) vs. directional penalty (r_{jk}), we applied the following normalization on r_{jk}:

$$\sum_k \log_{10} r_{jk} = 0 \quad (8)$$

where the base-10 logarithm of r_{jk} for all four voxel directions must sum up to 0. Such normalization ensures that increased weight in one direction would result in decreased weights in other directions, thereby keeping the overall smoothness approximately constant for a given β_j.

For the joint optimization of TCM and regularization, a Covariance Matrix Adaptation Evolution Strategy (CMA-ES) algorithm was adopted based on an open-source Python implementation [21]. A population size of 40 was used for each iteration and the convergence criterion is a change less than 10^{-5} in the objective function ($-d'^2$) value.

III. Implementation on an Experimental CBCT Bench

A. Experimental CBCT bench

The experimental CBCT bench used in these studies is illustrated in Fig. 4(a). The x-ray tube had a rotating tungsten anode and Sapphire housing (Rad94, Varian Medical Systems, CA), powered by a 80kW generator (Communications & Power Industries, Canada). The flat-panel detector (PaxScan 4343CB, Varian Medical Systems, CA) has a 600 μm CsI scintillator, native pixel pitch of 0.139 mm operating in 2x2 readout mode. A computer controlled motion system operates the linear stages (Velmex, NY) used for setting the system geometry, and a hexapod was used to rotate the object (ALIO industries, CO).

The system geometry was set to a source-detector distance of 104 cm and a source-axis distance of 85 cm. The acquisition involved 360 projections over 360°. Tube current modulation was achieved through pulse width modulation at a fixed tube current using a custom-modified automatic exposure control (AEC) interface.

B. Imaging task and phantom

The imaging phantom and task is shown in Fig.4(b). The elliptical shell (major axis = 25.5 cm, minor axis = 14.0 cm, height = 8.8 cm, thickness = 3.5 mm) was 3D-printed using a commercial grade 3D printer (Makerbot Replicator 2, Makerbot Industries, NY) and filled with water.

The stimuli consisted of three 1/16" acetal spheres equally distributed along the circumference of a ~2.31 mm radius circle. Two of such stimuli was constructed – each resting on top of a cylindrical epoxy support (EasyCast, Environmental Technology Inc., CA). The locations of the two stimuli were approximately symmetric about the short axis of the ellipse. The imaging task was formulated as the discrimination between the three spheres (e.g., a cluster of calcification) against one larger lesion (e.g., a larger Gaussian). To compute the task function, the stimuli were first modeled digitally. Assuming all rotational orientations of the cluster are equally likely, the task function was then calculated as the difference between the Hankel transform of the three spheres and a Gaussian of width 1.96 mm. The width of the Gaussian was chosen such that its 50% peak value occurs at the radius of the cluster (2.31 mm). The task function is plotted in Fig.4(c).

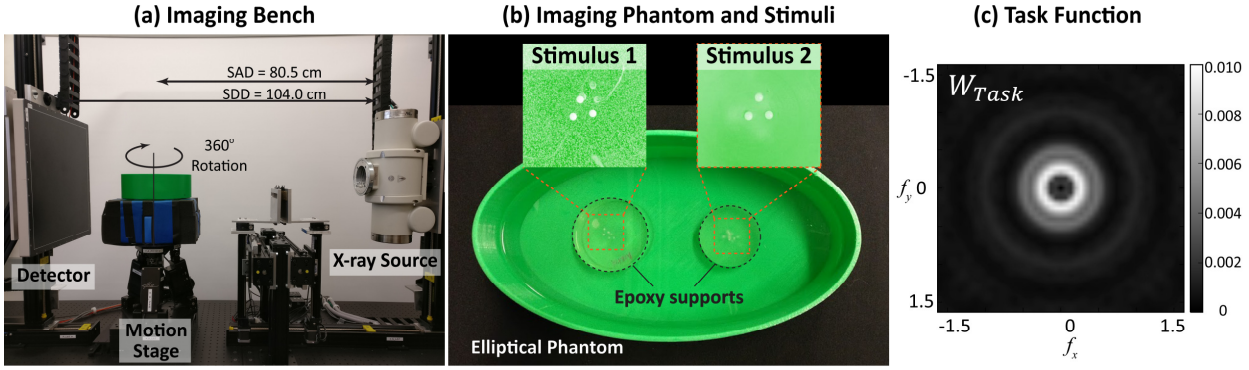

Fig.4. (a) Experimental CBCT imaging bench. (b) Elliptical phantom with a 3D printed shell and filled with water. Two stimuli simulating calcification clusters, each consisting of three 1/16" acetal spheres, are placed on top of epoxy supports and submerged in water. (c) The imaging task was formulated as the discrimination of the three separate spheres vs. a larger Gaussian. Assuming all rotational orientations of the cluster were equally likely, the resulting task function is shown in (c).

C. Imaging Strategies

To compare the performance of the task-driven imaging framework with conventional methods, we performed acquisitions and reconstructions for four strategies below:

1) Unmodulated: The fluence is constant for all projections.

2) Minimum FBP Variance ($\alpha = 0.5$): From Gies. et al. [15], the TCM pattern which results in minimum pixel variance in an FBP reconstruction is given by:

$$I_0(\theta) = \frac{e^{0.5 l_{j,\theta}}}{\sum_n e^{0.5 l_{j,\theta_n}}} I_{tot} \qquad (9)$$

where $l_{j,\theta}$ is the line integrals passing voxel j at projection angle θ calculated from the scout image.

To present a fair comparison of 1) and 2) with the task-driven strategies below, the overall penalty strength, β_j, were optimized for both strategies through an exhaustive search using d'_j as the objective.

3) Task-driven $I_0(\theta)$: Data were acquired using task-driven TCM and reconstructed using the optimal β_j only.

4) Task-driven $I_0(\theta) + r_{jk}$: Data were acquired using task-driven TCM and reconstructed using both optimal β_j and r_{jk}.

D. Tomographic data acquisitions

The nominal imaging techniques were set to 90 kV and 10 mA for all acquisitions. Pulse width for individual exposures (for each projection view) was used as a substitute for TCM. This permitted control of the exposure (mAs/frame) in each view corresponding to the fluence term (I_0) in both Eq.(6) and Eq.(9) for TCM and in Eq.(7) for the total fluence/dose constraint. A 3D scout image was acquired at a constant pulse width and reconstructed using FBP. For initial investigations in this work, the scout was taken at a higher dose level (90kV, 10mA, 40ms) and the locations of the two stimuli were identified. Using an ultra-low dose 3D scout for design purposes is the subject of an ongoing investigation.

Acquisitions for the four imaging strategies were performed for different total dose / pulse width levels, and reconstructions from two total dose levels (total mAs = 18.8 and 21.5) are shown in Sec.IV. For each dose level and imaging strategy, three repeated acquisitions were performed in order to account for the effect of different noise realizations on lesion detectability.

E. Gain correction for mAs modulated projection data

Proper gain correction is important for avoiding bias in PL reconstruction, especially for acquisitions involving TCM. We developed the following gain correction method to account for two potential sources of mismatch between commanded and delivered pulse width: 1) a systematic bias due to our customization of the x-ray generator, and 2) potential differences between pulse width delivered at a steady state (i.e., multiple exposures using the same pulse width) and pulse width delivered in a dynamically modulated scan[1]. To address the first, a one-time calibration step was performed to determine the relationship between the commanded pulse width vs. the delivered pulse width. A range of pulse widths from 0.1 ms to 30 ms was commanded for a single exposure acquisition, and a silicon diode (Accu-Pro, RadCal Corporation, CA, USA) was used to measure the delivered pulse width. Using this relationship, we address the second issue by a multipoint gain correction method where 30 repeated flat field images were acquired at a range of pulse widths from 0.01ms to 27.5ms. The flat field images were dark-corrected and averaged at each pulse width to obtain: 1) the mean readout signal in an arbitrary region of interest (ROI) vs. the actual pulse width, $\overline{I_{ROI}}(ms)$, and 2) the response for each pixel (assuming linear), $I_0(u,v) = a(u,v) * ms + b(u,v)$. To perform gain correction, each projection was first dark-corrected. An air region was identified and its mean readout was fitted to 1) to find the actual ms delivered for that projection. The gain image can then be calculated using 2).

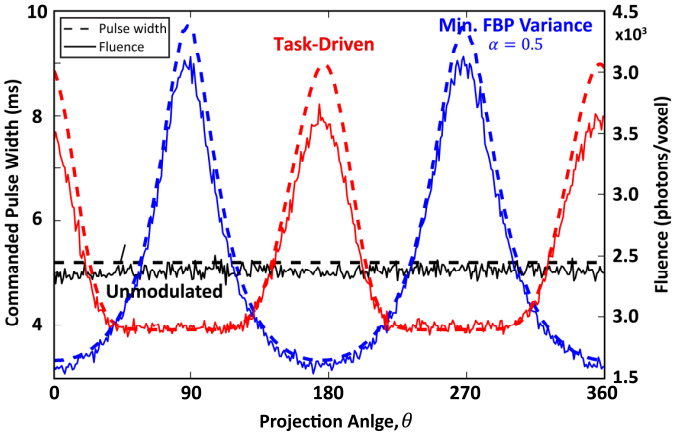

Fig.5. Tube current modulation profiles for the Unmodulated, Min. FBP Variance, and Task-Driven strategies. The dotted line represent commanded pulse width while the solid lines are delivered fluence calculated based on Poisson statistics. Opposite to the Min. FBP Variance strategy, the Task-Driven TCM assigns more fluence to the less attenuating views through the short axis of the ellipse (0°, 180°, and 360°)

F. Image reconstruction

Image reconstruction was performed using a custom GPU-enabled software package. The separable footprint forward- and back-projectors were employed. A combination of Nesterov momentum updates and subsets [22] were used for further speedup. A total of 40 iterations were performed. An isotropic voxel size of 0.3x0.3x0.3 mm was used.

IV. Results

The pulse width calibration from single exposure acquisitions suggested that there was a consistent 2.21 ms offset between the commanded and delivered pulse width (delivered = commanded + 2.21ms). This offset was accounted for during the design process. For all results below, "commanded" pulse width will refer to the value corrected by the systematic offset. The TCM profiles for the Unmodulated, Min. FBP Variance ($\alpha = 0.5$), and Task-Driven cases for stimulus 1 at a nominal total mAs of 18.8 or pulse width of 5.21 per projection are plotted in Fig.5. Optimization for both Task-Driven strategies yield very similar TCM profiles, so the same acquisition was used for both. Due to the symmetry of the elliptical phantom,

[1] It is possible to correct for this effect through additional calibration and modified control strategy.

the locations of the two stimuli, as well as a low magnification geometry, the TCM profiles for the two stimuli are very similar. Hence, only one set of acquisitions was performed for both stimuli.

The dotted lines represent the commanded pulse width, and the solid line represent the delivered fluence per pixel calculated from an air region in the gain-corrected/normalized projection data of one of the three repeated scans. Assuming Poisson noise, the fluence per pixel is calculated as the ratio of mean over variance of an air ROI in each projection. The delivered fluence generally follows the trends of the commanded pulse width, but with slightly lower peaks. The total fluence over all projections are approximately constant at $8.54\text{x}10^6$, $8.46\text{x}10^6$, and $8.53\text{x}10^6$ for the Unmodulated, Min. FBP Variance, and Task-Driven cases, respectively.

The Min. FBP Variance profile and the Task-Driven profiles exhibit the opposite trends. Note that projections angled around 0^o, 180^o, and 360^o correspond to the "AP view" of the ellipse (traversing the short axis), and projections around 90^o and 270^o correspond to the "lateral view" (traversing the long axis). For FBP reconstruction, the Min. FBP Variance strategy minimizes noise by assigning more fluence along the noisier lateral views. This TCM is also close to optimal for task-based performance in FBP [12]. For PL reconstruction, however, the optimal TCM is reversed with more fluence distributed along the less noisy views. This behavior can be explained by the lower statistical weighting associated with noisier data, which results in greater smoothing by the smoothness prior. Therefore, more fluence to noisier data would not result in a big noise advantage as the case for FBP, while increasing fluence in less noisy views brings

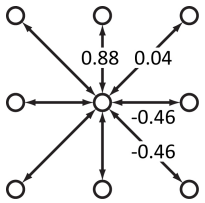

Fig.6. Optimal directional penalty shown as log10 exponent for the Task-Driven $I_0(\theta) + r_{jk}$ strategy. The directional penalty reinforces the same trend as TCM, where noisier voxels along y due to the lateral views are smoothed more and less noisy data along x are smoothed less.

greater benefit to detectability by boosting the spatial resolution in their radial directions and increasing signal power. The optimal directional penalty (Fig.6) reinforces the same trend, where noisier voxels in the y-direction (as a result of lateral views) while voxels in the x-direction are smoothed less. As shown in previous work [17], [23], the optimal β_j for each strategy mainly serves to match the spatial resolution in the reconstruction to approximately the frequency extent of the task function. For strategies 1~4, the optimal β_j are $10^{5.36}$, $10^{4.94}$, $10^{5.76}$, and $10^{5.24}$ for 18.8 total mAs case, and $10^{5.48}$, $10^{4.88}$, $10^{5.85}$, and $10^{5.36}$ for the 21.5 total mAs case.

Reconstructions of the stimuli 1 and 2 are shown in Fig.7 for two nominal dose levels (18.8 and 21.5 total mAs). The same ROIs in a high dose (40 ms per projection, unmodulated) PL reconstruction was also shown as a reference for the size and location of the stimuli. The relative d' of each strategy to the Unmodulated case, d'_{rel}, are overlaid for each dose level and stimulus. The Min. FBP Variance strategy has a d'_{rel} less than 1, indicating worse performance than the Unmodulated strategy. The two Task-Driven Strategies outperforms the rest, and the Task-Driven $I_0(\theta) + r_{jk}$ strategy being the best among the four. While a more sensitive and quantitative method (e.g.,

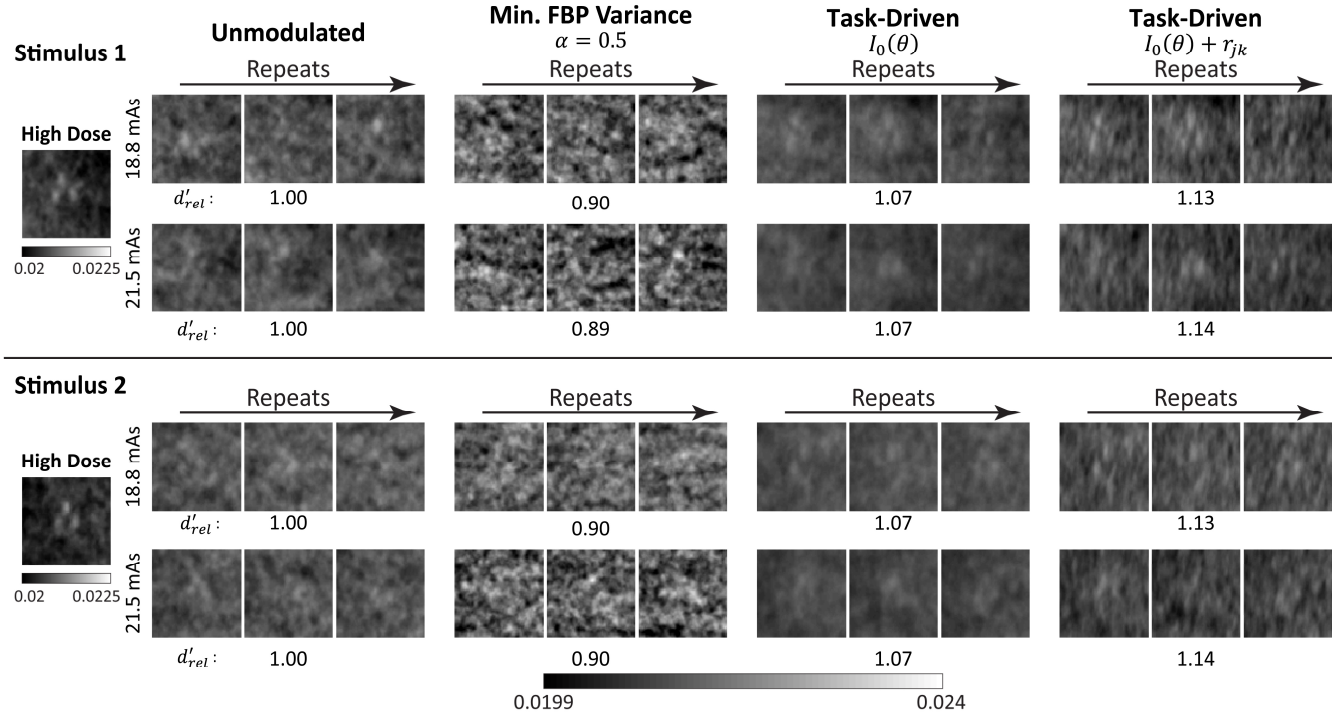

Fig. 7. Reconstruction ROIs for the four strategies containing stimulus 1 and 2 at two different dose levels. References ROIs are shown from a high dose, unmodulated PL reconstruction at the same location. The d' relative to the Unmodulated case, d'_{rel}, is shown for each stimulus and dose level. Visual inspection of the reconstructions support the trends of the d'_{rel} values. The stimuli are very challenging to see all of the Min. FBP Variance ROIs, are visible in a few of the Unmodulated ROIs, and are most easily identified in the Task-Driven reconstructions.

observer study) may be required to validate the d' values, visual inspection of the multiple repeats in each strategy shows strong evidence to support the d'_{rel} trend. It is very challenging to visualize the stimuli in any of the reconstruction ROIs following the Min. FBP Variance strategy. The Unmodulated case is qualitatively better, where the stimuli is visible in perhaps ~4 out of the 12 ROIs. The two Task-Driven strategies outperform both, with the stimuli visible in at least 7 out of the 12 ROIs. The difference between the two task-driven strategies is difficult to tell from visual inspection alone and the relatively small number of repeats.

V. Discussion and Conclusions

This work investigates TCM and regularization designs for PL reconstruction using a task-driven imaging framework. The TCM acquisitions were achieved on an experimental CBCT bench with custom modified AEC interface capable of pulse width modulation at fixed tube current and tube voltage as a function of projection angle. The task-driven design was performed for a cluster discrimination task in an elliptical water phantom. Two conventional acquisition strategies were also implemented for comparison. Visual inspection of the reconstructions suggests that Task-Driven strategies outperform the Unmodulated acquisition, and that the traditional TCM profile that is close to optimal for FBP reconstruction performs *worse* than an unmodulated acquisition when conducting PL reconstruction.

Future work will focus on two areas. First, a low dose scout will be used as the anatomical model for the task-driven imaging framework. The extent to which line integrals can be calculated based on a low dose reconstruction will likely depend on the complexity of the phantom. Another implication for using a low dose scout is that the nature and the location of the imaging task may not be known beforehand. In that case, uncertainties in the imaging task and task location need to be included in the optimization. Since the optimal fluence modulation depends on the local attenuation characteristics of the phantom, TCM alone cannot sufficiently cater to multiple locations. In that case, task-driven dynamic fluence field modulation design may implemented on the same imaging bench. Second, the system model for noise and resolution prediction invokes simplifying assumptions such as no detector blur and zero electronic noise. Future implementations of the framework will incorporate a more realistic system model [24] taking these factors into account. While the overall TCM trends are not expected to change, including detector blur and additive noise will likely lead to a more accurate β design.

In summary, initial investigations in this work show strong evidence in experimental data that the task-driven imaging framework outperforms conventional acquisition and reconstruction strategies. Moreover, conventional TCM strategies that are currently in clinical use can actually perform worse than an unmodulated acquisition for specific imaging tasks when MBIR is used. These observations suggest that current imaging strategies should be re-evaluated based on the reconstruction algorithm and processing chain, with likely impact on the required exposure settings for equivalent task performance between reconstruction methods.

References

[1] C. H. McCollough, A. N. Primak, N. Braun, J. Kofler, L. Yu, and J. Christner, “Strategies for Reducing Radiation Dose in CT,” *Radiol. Clin. North Am.*, vol. 47, no. 1, pp. 27–40, 2009.

[2] P. Prakash, W. Zbijweski, G. J. Gang, Y. Ding, J. W. Stayman, J. Yorkston, J. A. A. Carrino, and J. H. Siewerdsen, “Task-based modeling and optimization of a cone-beam CT scanner for musculoskeletal imaging,” *Med. Phys.*, vol. 38, no. 10, pp. 5612–5629, 2011.

[3] S. S. Hsieh and N. J. Pelc, “The feasibility of a piecewise-linear dynamic bowtie filter,” *Med. Phys.*, vol. 40, no. 3, p. 31910, 2013.

[4] T. P. Szczykutowicz and C. A. Mistretta, “Design of a digital beam attenuation system for computed tomography: part I. System design and simulation framework.,” *Med. Phys.*, vol. 40, no. 2, p. 21905, Feb. 2013.

[5] J. W. Stayman, A. Mathews, W. Zbijweski, G. Gang, J. H. Siewerdsen, S. Kawamoto, I. Blevis, and R. Levinson, “Fluence-field modulated x-ray CT using multiple aperture devices,” in *SPIE Medical Imaging*, 2016, p. 97830X–97830X.

[6] M. K. M. Kalra, M. M. Maher, T. T. L. Toth, B. Schmidt, B. L. Westerman, H. T. Morgan, and S. Saini, “Techniques and applications of automatic tube current modulation for CT 1,” *Radiology*, vol. 233, no. 3, pp. 649–657, Dec. 2004.

[7] M. Mcnitt-gray, “Tube Current Modulation Approaches : Overview , Practical Issues and Potential Pitfalls Tube Current Modulation - Overview.” 2011.

[8] M. Beister, D. Kolditz, and W. A. Kalender, “Iterative reconstruction methods in X-ray CT,” *Phys. medica*, vol. 28, no. 2, pp. 94–108, 2012.

[9] P. J. Pickhardt, M. G. Lubner, D. H. Kim, J. Tang, J. A. Ruma, A. M. del Rio, and G.-H. Chen, “Abdominal CT with model-based iterative reconstruction (MBIR): initial results of a prospective trial comparing ultralow-dose with standard-dose imaging,” *Am. J. Roentgenol.*, vol. 199, no. 6, pp. 1266–1274, 2012.

[10] M. Katsura, I. Matsuda, M. Akahane, J. Sato, H. Akai, K. Yasaka, A. Kunimatsu, and K. Ohtomo, “Model-based iterative reconstruction technique for radiation dose reduction in chest CT: comparison with the adaptive statistical iterative reconstruction technique,” *Eur. Radiol.*, vol. 22, no. 8, pp. 1613–1623, 2012.

[11] J. W. Stayman and J. H. Siewerdsen, “Task-based trajectories in iteratively reconstructed interventional cone-beam CT,” in *Proceedings of 12th International Meeting on Fully Three-Dimensional Image Reconstruction in Radiology and Nuclear Medicine*, 2012, pp. 257–260.

[12] G. J. Gang, J. W. Stayman, T. Ehtiati, and J. H. Siewerdsen, “Task-driven image acquisition and reconstruction in cone-beam CT.,” *Phys. Med. Biol.*, vol. 60, no. 8, pp. 3129–50, Apr. 2015.

[13] G. J. Gang, J. W. Stayman, W. Zbijweski, and J. H. Siewerdsen, “Task-based detectability in CT image reconstruction by filtered backprojection and penalized likelihood estimation,” *Med. Phys.*, vol. 41, no. 8, 2014.

[14] G. J. Gang, J. H. Siewerdsen, and J. W. Stayman, “Task-driven tube current modulation and regularization design in computed tomography with penalized-likelihood reconstruction,” in *SPIE Medical Imaging*, 2016, p. 978324.

[15] M. Gies, W. A. Kalender, H. Wolf, C. Suess, and M. T. Madsen, “Dose reduction in CT by anatomically adapted

tube current modulation. I. Simulation studies," *Med. Phys.*, vol. 26, no. 11, p. 2235, 1999.

[16] M. D. Harpen, "A simple theorem relating noise and patient dose in computed tomography," *Med. Phys.*, vol. 26, no. 11, p. 2231, 1999.

[17] G. J. Gang, J. H. Siewerdsen, and J. W. Stayman, "Task-driven optimization of CT tube current modulation and regularization in model-based iterative reconstruction," *Phys. Med. Biol.*, vol. Submitted, 2016.

[18] J. A. Fessler, "Mean and variance of implicitly defined biased estimators (such as penalized maximum likelihood): applications to tomography.," *IEEE Trans. Image Process.*, vol. 5, no. 3, pp. 493–506, Jan. 1996.

[19] J. W. Stayman and J. A. Fessler, "Efficient calculation of resolution and covariance for penalized-likelihood reconstruction in fully 3-D SPECT.," *IEEE Trans. Med. Imaging*, vol. 23, no. 12, pp. 1543–56, Dec. 2004.

[20] Y. Zhang-O'Connor and J. A. Fessler, "Fast predictions of variance images for fan-beam transmission tomography with quadratic regularization.," *IEEE Trans. Med. Imaging*, vol. 26, no. 3, pp. 335–46, Mar. 2007.

[21] N. Hansen and S. Kern, "Evaluating the CMA evolution strategy on multimodal test functions," in *International Conference on Parallel Problem Solving from Nature*, 2004, pp. 282–291.

[22] D. Kim, S. Ramani, and J. A. Fessler, "Accelerating X-ray CT ordered subsets image reconstruction with Nesterov's first-order methods," in *Proc. Intl. Mtg. on Fully 3D Image Recon. in Rad. and Nuc. Med*, 2013, pp. 22–25.

[23] G. J. Gang, J. H. Siewerdsen, and J. W. Stayman, "Task-Based Design of Fluence Field Modulation in CT for Model-Based Iterative Reconstruction," in *Proceedings of the 4th International Conference on Image Formation in X-Ray Computed Tomography*, 2016, pp. 407–410.

[24] W. Wang, G. J. Gang, and J. W. Stayman, "Spatial resolution properties in penalized-likelihood reconstruction of blurred tomographic data," in *Fully 3D Meeting*, 2017, p. Submitted.